# Equation of State Predictions for ScF<sub>3</sub> and CaZrF<sub>6</sub> with Neural Network-Driven Molecular Dynamics

John P. Stoppelman, Angus P. Wilkinson, 1, 2 and Jesse G. McDaniel 1

<sup>1)</sup>School of Chemistry and Biochemistry, Georgia Institute of Technology, Atlanta, Georgia 30332-0400, USA

<sup>2)</sup>School of Materials Science and Engineering, Georgia Institute of Technology, Atlanta, Georgia 30332-0245, IISA

(\*Electronic mail: mcdaniel@gatech.edu)

(Dated: 21 July 2023)

In silico property prediction based on density functional theory (DFT) is increasingly performed for crystalline materials. Whether quantitative agreement with experiment can be achieved with current methods is often an unresolved question, and may require detailed examination of physical effects such as electron correlation, reciprocal space sampling, phonon anharmonicity, and nuclear quantum effects (NQE), among others. In this work, we attempt first-principles equation of state prediction for the crystalline materials ScF<sub>3</sub> and CaZrF<sub>6</sub> which are known to exhibit negative thermal expansion (NTE) over a broad temperature range. We develop neural network (NN) potentials for both ScF<sub>3</sub> and CaZrF<sub>6</sub> trained to extensive DFT data, and conduct direct molecular dynamics (MD) prediction of the equation(s) of state over a broad temperature/pressure range. The NN potentials serve as surrogates of the DFT Hamiltonian with enhanced computational efficiency allowing for simulations with larger supercells and inclusion of nuclear quantum effects utilizing path integral approaches. The conclusion of the study is mixed: while some equation of state behavior is predicted in semiquantitative agreement with experiment, the pressure-induced softening phenomenon observed for ScF<sub>3</sub> is not captured in our simulations. We show that NQE have a moderate effect on NTE at low temperature, but do not significantly contribute to equation of state predictions at increasing temperature. Overall, while the NN potentials are valuable for property prediction of these NTE (and related) materials, we infer that a higher level of electron correlation, beyond the GGA density functional employed here, is necessary for achieving quantitative agreement with experiment.

#### I. INTRODUCTION:

In silico prediction of the stability and properties of inorganic materials has become possible on a broad scale due largely to density functional theory (DFT) and associated advancements in algorithms, software, and computer hardware.<sup>1</sup> With exception, the majority of such efforts focus on crystalline materials, for which the lattice structure is either known or postulated, and entropic contributions to the free energy may be approximated or sometimes neglected. Example efforts include structure prediction,<sup>2</sup> prediction of mechanical properties,3 discovery of battery, photovoltaic, or thermoelectric materials,<sup>4</sup> stability prediction of alloy structures or polymorphs,<sup>5</sup> or screening for stable, ternary inorganic materials,<sup>6</sup> In this work, we attempt first-principles equation of state prediction for ScF<sub>3</sub> and CaZrF<sub>6</sub> inorganic crystals, which fall under the class of negative thermal expansion (NTE) materials.

Negative thermal expansion (NTE) materials are of significant interest due to both their unusual physics and their potential applications. Numerous applications require matching coefficients of thermal expansion between two or more materials, and the discovery of new NTE materials and elucidation of their behavior provides greater tunability in this design space. Examples of possible uses for NTE materials include fuel cells, mirrors in space telescopes, optics, thermoelectric materials and more. The discovery of new NTE materials as well as better fundamental understanding of documented NTE behavior are both important goals. Regarding the latter, predicting/rationalizing NTE behavior from first-

principles is often challenging and may serve as a stringent test of solid-state theories, particularly those focused on incorporating phonon anharmonicity.

A variety of mechanisms can cause NTE, and thus it is observed in several classes of compounds, such as ferroelectric materials, <sup>10</sup> MOFs, <sup>11</sup> Prussian Blue analogues <sup>12</sup> and other open-framework materials.<sup>7,13</sup> The work of Mary et al. <sup>14</sup> on ZrW<sub>2</sub>O<sub>8</sub> documenting NTE over a wide temperature range, launched interest into framework-type materials. 15 Due to their simpler structure in comparison to ZrW2O8, ReO3type materials are of interest for fundamental understanding of NTE behavior in open framework structures. 16-19 While ReO<sub>3</sub> itself only shows small NTE at low temperatures, Greve et al. <sup>19</sup> found that ScF<sub>3</sub>, which possesses a ReO<sub>3</sub>-type structure, displays strong NTE from 10 K up to  $\sim$  1100 K with a coefficient of thermal expansion (CTE) of  $\alpha_L \sim -14$  ppm/K at 100 K. In most metal trifluorides, the rhombohedral  $(R\bar{3}c)$ phase is more stable than the cubic  $(Pm\bar{3}m)$  phase at low temperatures and elevated pressures, which leads to positive thermal expansion; in contrast, for ScF<sub>3</sub>, the cubic phase is more stable than the rhombohedral at low temperature and ambient pressure, which leads to NTE. 19-21 The discovery of strong NTE in ScF<sub>3</sub> has led to further research into its other properties, such as pressure-induced softening,<sup>22</sup> which causes a material to become more compressible with increasing pressure, and methods for controlling its thermal expansion. Yang et al. <sup>23</sup> observed a reduction of NTE upon formation of ScF<sub>3</sub> crystals with grain sizes of 80 nm. Similarly, Hu et al. 24 synthe sized  $\sim 6$  nm ScF<sub>3</sub> crystals for which only positive thermal expansion was observed. Further strategies for tuning thermal expansion with ScF<sub>3</sub> include the formation of solid solutions through isovalent cation substitution,  $^{25-29}$  redox intercalation of cations into the ScF<sub>3</sub> A-sites  $^{30}$  and the introduction of excess fluoride through aliovalent cation substitution.  $^{31,32}$  CaZrF<sub>6</sub> is another open-framework material with ReO<sub>3</sub>-type structure that displays NTE, and exhibits a more negative CTE ( $\alpha_L \sim -18$  ppm/K at 100 K) than ScF<sub>3</sub>.  $^{33}$  The NTE behavior of CaZrF<sub>6</sub> can be modulated in various ways; for example, incorporation of helium under high-pressure gas has been shown to create a defect perovskite (He<sub>2-x</sub>□<sub>x</sub>)(CaZrF<sub>6</sub>)  $^{34}$  and a stoichiometric hybrid perovskite [He<sub>2</sub>][CaZrF<sub>6</sub>],  $^{35}$  with different equations of state.

Computational and theoretical work on NTE materials may be categorized based on goals: The first category consists of theoretical work that seeks to rationalize and develop physical understanding of NTE phenomenon, often through simplified models. The second category is computational work which targets quantitative, in silico property prediction, utilizing e.g. DFT or higher accuracy electronic structure methods. The present work falls into the latter category, as we target (although do not fully achieve) quantitative, equation of state prediction for ScF3 and CaZrF6 NTE materials utilizing first-principles, computational methods. There is of course synergy between these categories of efforts. In computational predictions, necessary choices about what "physics to include" should be made based on the insight gleaned from simplified models. On the other hand, state-of-the-art computational predictions are important for testing and validating the approximations made in simplified models, and providing benchmarks when experimental data is unavailable.

We first discuss theoretical efforts and simplified models which have largely provided the physical understanding and insight into NTE behavior. 18,36-40 The rigid unit vibrational mode (RUM) model is a representative approach belonging to this category and has provided mechanistic analysis into framework NTE materials. 18,37,41-43 In the context of these materials, RUMs are low-frequency modes that engage in cooperative rotations of octahedral units; the motions associated with these modes involve minimal distortion of these octahedral geometries. The RUM model was initially applied to understand phase transitions in silicates and first applied to framework NTE materials with studies of ZrW<sub>2</sub>O<sub>8</sub>. 42,44,45 In ScF<sub>3</sub>, the RUMs (along with quasi-RUMS, modes with wavevectors close to the RUMs) have been demonstrated in the literature to be the key modes for NTE in ScF<sub>3</sub>. 46,47 Analysis of the phonon spectrum of CaZrF<sub>6</sub> indicates that the RUM model is applicable for this system as well.<sup>48</sup>

*Ab initio* methods have been used for both mechanistic analysis and attempted quantitative prediction, and we summarize those studies focusing on ScF<sub>3</sub> or CaZrF<sub>6</sub>. Several works have investigated NTE in ScF<sub>3</sub> with DFT-based approaches, utilizing either vibrational free energy predictions or *ab initio* molecular dynamics (AIMD) simulations. Oba *et al.* <sup>49</sup> evaluated quasiharmonic approximation (QHA)<sup>50</sup> free energy expressions for ScF<sub>3</sub>, and found that QHA predicts qualitatively incorrect behavior. This is likely due to the fundamental importance of anharmonicity in NTE systems, requiring extensions beyond harmonic treatments.<sup>51</sup> Meth-

ods that go beyond the QHA have been used to study ScF<sub>3</sub>, such as the self-consistent phonon theory (SCP), which includes quartic anharmonicity, 52,53 and the improved selfconsistent phonon theory (ISC), which additionally treats cubic anharmonicity.<sup>54</sup> These procedures require parameterization of high-order force constants from first-principles calculations.<sup>55,56</sup> In contrast, AIMD is straightforward and naturally takes into account anharmonicity. AIMD simulations have been conducted for ScF<sub>3</sub>, providing insight into its NTE behavior. 51,57-59 Utilizing AIMD, Lazar, Bučko, and Hafner <sup>57</sup> were able to reproduce the NTE effect over a temperature range of 200K - 800K using a  $2 \times 2 \times 2$  supercell of the cubic phase. They demonstrated the pressure dependence of NTE in ScF<sub>3</sub> and related this to the stability of the  $R\bar{3}C$ phase. Bocharov et al. 58 investigated the CTE and dynamics of ScF<sub>3</sub> at different supercell sizes. They found that at least a  $4 \times 4 \times 4$  supercell for ScF<sub>3</sub> is needed to converge AIMD predictions with system size, due to the long wavelength phonons with negative Grüneisen parameters accounting primarily for NTE behavior.<sup>24,58</sup> As CaZrF<sub>6</sub> is a more complicated material, there are fewer *ab initio* studies in the literature. <sup>60,61</sup> Gupta et al. 60 used the QHA to study CaZrF<sub>6</sub> and related systems, and again demonstrated the importance of anharmonicity for modeling thermal expansion effects.

While AIMD is a powerful technique, its high computational cost makes it of limited use for equation of state prediction on a general scale. As discussed, larger supercells are often necessary to avoid finite size effects associated with longwavelength/low frequency phonons that make important contributions to NTE, and the computational expense of AIMD makes simulation of such supercells challenging.<sup>33</sup> Additionally, nuclear quantum effects (NQE) may be important, requiring computationally expensive path integral simulations. As an example, consider the phonon spectra of CaZrF<sub>6</sub> discussed by Hancock et al. 33. The high frequency phonons typically have positive Grüneisen parameters  $(\gamma)$ , whereas low frequency modes exhibit negative  $\gamma$ , the latter contributing to NTE. While a classical treatment is expected to work well for low frequency (e.g.  $\leq 200 - 300 \text{ cm}^{-1}$ ) modes, quantization will be important for high frequency modes; a classical treatment will incorrectly assign energy equipartition to these high frequency modes and thus tend to underestimate NTE effects at lower temperatures.<sup>49</sup> Combining path integral approaches with AIMD may often be computationally intractable for systems of interest. Alternatives include fitting molecular mechanics force fields to quantum mechanical data.<sup>22</sup> For materials of increasing complexity, developing sufficiently accurate force fields is both a challenging and time consuming task.

Because of the discussed limitations, obtaining quantitatively accurate, *in silico* equation of state predictions may often require methods other than direct DFT-based AIMD. An emerging strategy is to use artificial neural networks or other machine learning methods to act as surrogate Hamiltonians that exhibit DFT-level (or higher) accuracy with substantially enhanced computational efficiency<sup>62,63</sup> Machine learning (ML) methods have been increasingly adopted in the chemistry and materials science community to simulate materials with *ab initio* accuracy at orders of magnitude lower

computational cost as compared to AIMD.<sup>64–66</sup> As long as a training set of high-quality reference data is available, usually consisting of ab initio energies/forces for the system of interest, ML techniques such as neural networks, kernel methods or other tools can be used to construct ML potentials.<sup>67</sup> These ML potentials can then be used to run molecular dynamics (MD) or Monte Carlo simulations to predict physical properties of interest. In particular, ML models have been used to study a large variety of materials, such as silicon, <sup>68,69</sup> various metal systems, <sup>70–72</sup> zeolites, <sup>73</sup> MOFs<sup>74</sup> and more. <sup>64,75</sup> ML techniques have also been used to screen materials such as MOFs, zeolites and perovskites for selected applications. 76–78 In this work, we develop similar ML potentials for the NTE materials ScF<sub>3</sub> and CaZrF<sub>6</sub> to predict equations of state from direct MD simulations. These ML potentials allow for efficient MD simulations of large supercells, and additionally enable path integral molecular dynamics (PIMD) simulations that explicitly incorporate NQE.

In this work, we train NN potentials to a training set of DFT energy, force, and stress tensor calculations for ScF<sub>3</sub> and CaZrF<sub>6</sub> to enable direct MD prediction of the equations of state. We compare predictions for CTE, atomic displacement parameters, the bulk modulus, and additional equation of state data against both experiment and prior theoretical predictions. Utilizing PIMD simulations, we additionally quantify the contribution of NQE to the equations of state of these materials over a wide temperature range. Overall, the predictions from our NN-driven, MD simulations are generally in qualitative to semiquantitative agreement with experimental equation of state data. Our predictions underestimate the extent of negative thermal expansion, even when NQE are fully incorporated, and we speculate that this is likely due to deficiencies in the underlying density functional (training data). We find that NQE modulate the CTE by 30-60% at low temperature (100 K) for both materials, which is qualitatively consistent with findings from previous studies.<sup>49</sup> A particularly apparent discrepancy of our simulations is the missing pressure-induced softening effect for cubic ScF<sub>3</sub> which is observed experimentally.<sup>22</sup> Overall our study demonstrates both the utility and limitations of MD simulations utilizing NNs with underlying DFT-accuracy for equation of state predictions of NTE materials.

## II. METHODS:

## A. Training Set Generation and Model Training

We first describe our procedure for constructing a training dataset of DFT energies, forces and stress tensors for  $ScF_3$  and  $CaZrF_6$ . The training sets for both crystals were generated from *ab initio* geometry optimizations and AIMD simulations using the Quantum ESPRESSO package.<sup>79</sup> We used the Atomic Simulation Environment (ASE) package<sup>80</sup> to generate a  $4 \times 4 \times 4$  supercell for  $ScF_3$  and a  $2 \times 2 \times 2$  supercell for  $ScF_6$  from the cubic (primitive) unit cells obtained from the Materials Project.<sup>1</sup> The PBE density functional and PAW pseudopotentials were used for all calculations,<sup>81,82</sup> with  $\Gamma$ -

point sampling of the band structure in all cases. Suitable values for the plane wave cutoffs (kinetic energy/density) were determined from convergence tests of the stress tensor (which is typically harder to converge than energy/forces). These convergence tests are shown in Figures S1 and S2, and the final cutoff values employed were 180 Ry/ 1152 Ry for the kinetic energy/density for ScF<sub>3</sub> and 200 Ry/1200 Ry for the kinetic energy/density for CaZrF<sub>6</sub>.

AIMD simulations were conducted for both materials over a range of temperatures and pressures to generate training data. For  $ScF_3$ , we ran numerous  $\sim 1$  ps NPT simulations of the  $4 \times 4 \times 4$  supercell over a temperature range of 300 to 1600K and a pressure range of 0 to 800 MPa. 83 The timestep was set to 20 atomic units (approximately 1 fs). The Parrinello-Rahman method was used for pressure-coupling, with the fictitious mass set to the default value in Quantum ESPRESSO, and velocity rescaling was used for the thermostat. The velocities were rescaled every 5 timesteps. This resulted in a training set of energies, forces, and stress tensors for approximately 8500 ScF<sub>3</sub> cubic-phase structures of different coordinates and lattice parameters. We additionally generated training data for the rhombohedral phase of ScF<sub>3</sub> to explore how the inclusion of this training data altered the NN predictions (vide infra). We thus ran additional AIMD simulations for a  $2 \times 2 \times 2$  supercell of the rhombohedral conventional unit cell structure at 300 K and pressures ranging between 0-1000 MPa (the unit cell was obtained from the Materials Project<sup>1</sup>). This added training data for approximately 1200 ScF<sub>3</sub> rhombohedral structures of different coordinates and lattice parameters. For CaZrF<sub>6</sub>, training data was generated for the cubic phase only. AIMD simulations of  $2 \times 2 \times 2$ CaZrF<sub>6</sub> supercells were run over a temperature range of 300 -1400 K and a pressure range of 0 - 500 MPa. This resulted in a training set of energies, forces, and stress tensors for approximately 6000 CaZrF<sub>6</sub> cubic structures of different coordinates and lattice parameters.

The DeepMD architecture was utilized for the NN potentials, 84,85 and was trained to the energies, forces, and stress tensors comprising the training data for each material. Within the DeepMD architecture, an initial descriptor network converts the local environment of each atom into a set of embeddings that obey translational, rotational and permutational invariance, and a second network utilizes this embedding to predict the energy, forces, and virial of the system. 84 DeepMD's 'se\_2\_a' descriptor was used for the embedding network, which incorporates both radial and angular information. 86 Separate neural networks were trained for both ScF<sub>3</sub> and CaZrF<sub>6</sub>. The descriptor deep neural network was made up of three hidden layers using 25, 50 and 100 neurons. Neighbors within 8 Å were included in the local environment for each atom. For ScF<sub>3</sub>, the fitting net consisted of three hidden layers with 240 neurons each; for CaZrF<sub>6</sub>, the fitting net was reduced to 40 neurons each in order to balance accuracy and computational cost. A multi-target loss function balancing energy, force and stress loss between the reference data and the neural network was used in order to fit all three properties (see Wang et al. 84 and the Supplementary Material). We benchmarked the choice in weights used for each term in the

loss function to ensure our results were relatively insensitive; this is also included in the Supplementary Material. The initial learning rate for both neural networks was set to  $1\times 10^{-3}$  and ended at  $3.5\times 10^{-8}$ , with 5000 decay steps. A 80:20 split was used to construct a training and validation set from the total dataset; the test set was assembled from classical MD simulations using the final neural networks (the settings used for the simulations are described in the next section). Each model was trained for  $10^6$  steps for training and validation. The input files with all hyperparameters used to build the DeepMD models are included in the Supplementary Material.

Neural network potentials may become unstable during simulations, since spurious forces will be predicted if the system drifts far outside of the configuration space included in the training set.<sup>87</sup> Our initial AIMD simulations were of only 1 ps in length, which does not allow for sufficiently exploring all regions of phase space of interest in this work. We observed that the initially trained neural networks for both materials were unstable for high temperature (>1000 K) classical MD simulations after  $\sim 10$  ps. To fix this initial instability, we added additional training data consisting of Quantum ESPRESSO computed energies, forces, and stress tensors for structures taken from the NN simulation snapshots. The DeepMD NN potential was then re-trained to the expanded training set. This procedure was done iteratively until there were no observed instabilities while running MD with the NN potentials. In total, additional training data for approximately 1000 structures was added to the original training set for both materials within this iterative procedure. The NN simulation procedure is described in the next section (see the classical simulation details).

The final NN potentials were then tested as follows. MD simulations using these NN potentials were performed over a temperature range of 300 - 1000K and a pressure range of 0 to 300 MPa. A  $4 \times 4 \times 4$  supercell was used for the ScF<sub>3</sub> simulations and a  $2 \times 2 \times 2$  supercell was used for the CaZrF<sub>6</sub> simulations. Quantum ESPRESSO was used to compute the DFT energy, forces, and stress tensor for approximately 300 snapshots from these simulations. A comparison of the predicted neural network energy vs. DFT energy and forces on the test set for both materials is shown in Figures S4 and S5 of the Supplementary Material. For ScF<sub>3</sub>, the energy mean absolute error (MAE) is 0.042 eV (0.1 meV/atom) and the forces MAE is 0.02 eV/Å; to test the accuracy of the stress tensor, we computed the internal pressure from the stress tensor from both DFT and the neural network. The MAE is  $6.6 \times 10^{-5}$ eV/Å<sup>3</sup> (approximately 10 MPa). For CaZrF<sub>6</sub>, the energy MAE is slightly worse at 0.18 eV (0.7 meV/atom); however, as can be seen in Figure S4, there is little scatter in the predicted energies. The forces MAE is 0.033 eV/Å and the pressure MAE is  $7.2 \times 10^{-5}$  eV/Å<sup>3</sup> (approximately 11 MPa).

#### B. Neural Network-Driven, Molecular Dynamics Simulations

We perform MD simulations with the final NN potentials to predict equations of state for the ScF<sub>3</sub> and CaZrF<sub>6</sub> materials. Both classical MD and path integral PIMD simula-

tions were run in order to examine the impact of NQE; we explicitly denote which predictions correspond to each simulation type when discussing the results. All simulations were conducted using ASE with the DeepMD calculator. 80,84 The DeepMD architecture allows for simulations of supercells of arbitrary size, since the total energy of the system is represented as a sum of atomic energies. The majority of our calculations were performed on  $5 \times 5 \times 5$  supercells of ScF<sub>3</sub> and  $3 \times 3 \times 3$  supercells of CaZrF<sub>6</sub> (both in the cubic phase). As noted by Dove and Fang 43, simulations of ScF<sub>3</sub> with an odd number of unit cells will not entirely capture phonons associated with tilt modes along the M-R branch, which may be important to include. However, we have verified that predictions from our chosen supercells are largely converged with respect to system size, and choice of odd/even number of unit cells. In Figure S8, simulation predictions of larger supercells  $6 \times 6 \times 6$  and  $7 \times 7 \times 7$  for ScF<sub>3</sub> indicate that predictions from the smaller/odd numbered  $5 \times 5 \times 5$  ScF<sub>3</sub> supercell are largely converged. Similarly, in Figure S15, simulation predictions of the larger (and even numbered)  $4 \times 4 \times 4$  CaZrF<sub>6</sub> supercell are very close to the predictions from the smaller (and odd numbered)  $3 \times 3 \times 3$  CaZrF<sub>6</sub> supercell. Another factor for our specific choice of supercells  $(5 \times 5 \times 5)$  supercell for  $ScF_3$  and  $3 \times 3 \times 3$  supercell for  $CaZrF_6$  ) is based on preliminary simulations that employed a neural network trained to a dispersion-corrected density function; these preliminary predictions are shown in Figure S17, and show dramatic instabilities for systems of even numbered unit cells. This is discussed in more detail in Section III.

For computing the coefficient of thermal expansion  $(\alpha_L)$ , a series of simulations were run in the NPT ensemble using the isotropic Berendsen barostat.<sup>88</sup> A Berendsen thermostat was used for the temperature coupling. The simulations were run for  $\sim 4$  - 5 ns at a pressure of 0 MPa and temperatures ranging from 100 - 1200 K. We benchmark a different thermostat/barostat choice in the Supplementary Material Figure S6 using the i-Pi package (Langevin thermostat/Bussi-Zykova-Parrinello barostat);89 we observe converged results with our predictions. A time step of 1.0 femtosecond was used with a barostat time constant of 1.0 ps and a thermostat coupling constant of 1.0 ps. NPT simulations were conducted to compute pressure vs. volume curves for ScF<sub>3</sub>, starting from the  $5 \times 5 \times 5$  cubic supercell geometry. These simulations were run in the i-Pi package interfaced with ASE. Each simulation was run for 1 - 2 ns and performed over a pressure range of 0 to 500 MPa and temperature range of 55 to 240 K. A Langevin thermostat was used along with the MTK barostat. 90 A time constant of 1 ps was used for both the thermostat and barostat, and the time step was set to 1.0 fs.

Similar NPT simulations were run for  $CaZrF_6$ . Three main sets of properties were calculated for  $CaZrF_6$ . Thermal expansion was investigated between 100 and 1000 K at 0 MPa, similar to the  $ScF_3$  simulations. Then, volume vs. pressure curves were obtained from a set of simulations run at a temperature of 290 K and pressures from 0 to 300 MPa. Finally, the bulk modulus of  $CaZrF_6$  was computed over a temperature range of 300 to 500 K. A set of three simulations from 0 to 200 MPa was performed for each temperature. A linear fit to the aver-

age volume vs. pressure data from these simulations was used to compute the bulk modulus at each temperature. All CaZrF6 simulations were run for  $\sim$  1-2 ns. The Berendsen barostat with a 1.0 ps time constant was used for all simulations.

The i-Pi software package interfaced with ASE was utilized to run the path integral MD simulations. 91,92 Isotropic path integral NPT simulations were run for both systems. Simulations were run over a temperature range of 100 - 1200 K for cubic ScF<sub>3</sub> and a temperature range of 100 - 1000 K for cubic CaZrF<sub>6</sub>, and the pressure was fixed to 0 MPa. A smaller time step of 0.5 fs was used here. The barostat implementation details can be found in Bussi, Zykova-Timan, and Parrinello 89 and Ceriotti, More, and Manolopoulos 91 A time constant of 0.2 ps was used for the barostat. A standard Langevin thermostat was used for temperature coupling, with a time constant of 0.2 ps. Depending on temperature, between 5 to 15 beads were utilized for the path integral simulations of both ScF<sub>3</sub> and CaZrF<sub>6</sub>(with greater number of beads used for lower temperatures). Convergence tests of the lattice parameter with respect to number of beads are shown in Figure S9 and S16. Each PIMD simulation was run for 300-500 ps.

We briefly comment on the computational cost of our neural network vs. Born-Oppenheimer MD simulations performed with Quantum ESPRESSO. For example, 10 time steps of NPT simulation of the  $4\times4\times4$  ScF3 supercell with Quantum ESPRESSO on 96 cores (4 Dual Intel Xeon Gold 6226 processors) took 14,667 seconds (4 hours 4 minutes 27 seconds). With the neural network on a NVIDIA Tesla v100 GPU, a 10 time step simulation takes 1.86 seconds, which is about a 4 orders of magnitude difference in simulation time, demonstrating the utility of the approach for simulating larger crystals.

## III. RESULTS:

Our initial target is to investigate the extent to which the NN-driven MD simulations accurately predict the CTE for both ScF<sub>3</sub> and CaZrF<sub>6</sub>. Because the NN potentials exhibit essentially DFT-level accuracy (Section II A), our results should be interpreted as the accuracy to which the underlying density functional (PBE) describes the material properties.. In Figure 1, we plot the predicted thermal expansion behavior for ScF<sub>3</sub> and CaZrF<sub>6</sub> as computed from both classical MD (labeled as "NN") and PIMD simulations (labeled as "PI NN") utilizing the NN potentials. We plot both the temperature-dependent reduced lattice constant  $(a/a_0)$  and linear coefficient of thermal expansion: CTE =  $\frac{1}{a} \frac{da}{dT}$ ; these are plotted in Figure 1a and 1b for SeE and Figure 15. 1b for ScF<sub>3</sub> and Figure 1c and 1d for CaZrF<sub>6</sub>. In all cases, we plot corresponding experimental data and prior theoretical/computational predictions for comparison, where available. The curves are third order polynomials fit to the data points, with  $a_0$  taken as the extrapolated 0K value for a from the fitted polynomial for each set of data.

Inspection of Figure 1 indicates that the NN simulations indeed predict NTE for both systems, in qualitative agreement with experiment. Furthermore, the simulations correctly predict the experimental trend that the CTE is more negative for CaZrF<sub>6</sub> than ScF<sub>3</sub>. Experimentally, the CTE values

are  $\alpha_{100K,L} = -18$  ppm/K for CaZrF<sub>6</sub> and  $\alpha_{100K,L} = -14$  ppm/K for ScF<sub>3</sub> at 100 K. For comparison, the classical MD ("NN") simulations predict a CTE of  $\alpha_{100K,L} = -9.8$  ppm/K for CaZrF<sub>6</sub> and  $\alpha_{100K,L} = -4.3$  ppm/K for ScF<sub>3</sub> at 100 K. Incorporation of NQE within the PIMD simulations ("PI NN") brings the CTE values into closer agreement with experiment, with these simulations predicting  $\alpha_{100K,L} = -14.3$  ppm/K for CaZrF<sub>6</sub> and  $\alpha_{100K,L} = -8.7$  ppm/K for ScF<sub>3</sub> at 100 K. Thus NQE lower the CTE by  $\sim 30$ -60% at 100 K, while the influence of NQE diminishes at higher temperatures and largely disappears by temperatures of 700 K to 800 K. Overall, these results indicate that the MD simulations driven by DFT-trained NNs predict NTE behavior of ScF<sub>3</sub> and CaZrF<sub>6</sub> in semiquantitative to qualitative agreement with experiment.

Our CTE predictions for CaZrF<sub>6</sub> are comparatively better than for ScF<sub>3</sub> in that there is closer quantitative agreement with experiment. For CaZrF<sub>6</sub> the predicted CTE at 100 K is within a factor of 1.3 of the experimental value when incorporating NQE with the PIMD simulations (and a factor of 1.8 without NQE). There is no obvious reason for why the predictions for CaZrF<sub>6</sub> agree somewhat better with experiment compared to the predictions for ScF<sub>3</sub> (although as discussed later, the pressure-induced softening effect for ScF<sub>3</sub> is also not reproduced by our simulations). The influence of NQE on the CTE is consistent with the trend expected from analysis of the phonon spectrum. For both CaZrF<sub>6</sub> and ScF<sub>3</sub> materials, low frequency phonon modes exhibit negative Grüneisen parameters associated with NTE, while higher frequency phonons exhibit positive Grüneisen parameters. 33,93 A classical treatment will incorrectly assign energy equipartition to these high frequency modes and overpredict their contribution to (positive) thermal expansion at low temperatures.<sup>49</sup> Further inconsistencies of our simulation predictions with the experimental NTE behavior are predicted transitions from negative to positive thermal expansion at lower temperatures than those experimentally measured. As seen in Figure 1, our simulations for ScF<sub>3</sub> predict positive thermal expansion above temperatures of 600 K/700 K for MD/PIMD respectively, while the experimental crossover temperature is near 1100 K. For CaZrF<sub>6</sub>, a similar effect is observed, with the transition occurring at 900 K in both the classical MD and PIMD predictions, while solely NTE is experimentally observed over the full characterized temperature range.

We discuss possible reasons for the quantitative discrepancies between our thermal expansion predictions and the experimental data. Important considerations for *ab initio* equation of state prediction for these materials include: 1) phonon anharmonicity; 2) NQE; 3) finite-size effects; and 4) accuracy of the underlying density functional. Regarding 1), predictions from MD simulations explicitly incorporate full anharmonicity of phonon modes, in contrast to theoretical free energy models (*vide infra*). For 2), we have explicitly evaluated the influence of NQE, and NQE do not account for the remaining discrepancy with experiment; Figures S9 and S16 show that NQE are largely converged with respect to the number of beads used in the PIMD simulations. Regarding 3) finite-size effects, we have tested convergence of our predictions with respect to simulated supercell size. Figures S8 and S15

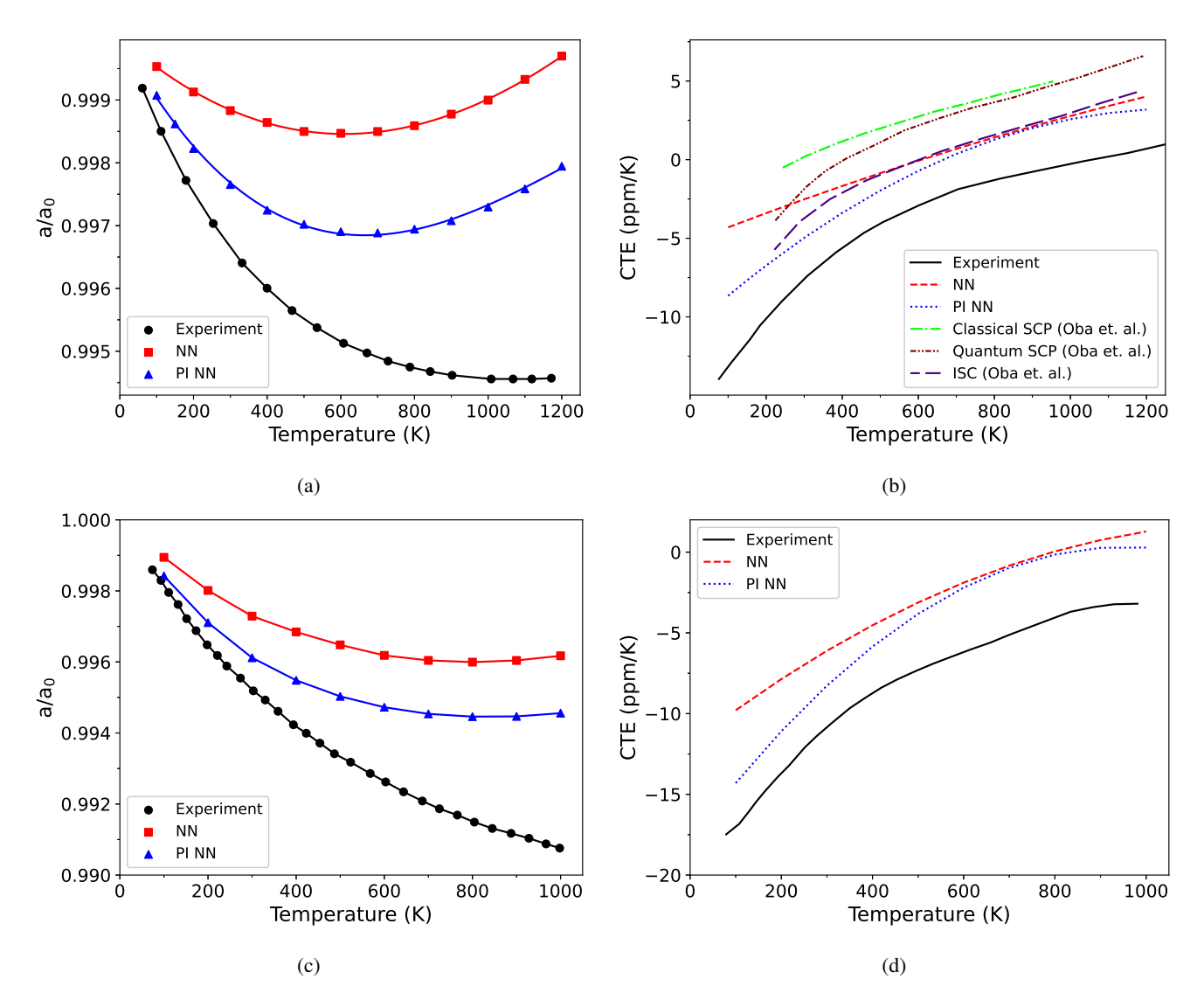


FIG. 1: Thermal expansion of  $ScF_3$  denoted by a) reduced lattice constant  $a/a_0$  and b) CTE. Thermal expansion of  $ScF_3$  denoted by c) reduced lattice constant  $a/a_0$  and d) CTE. The experimental results for  $ScF_3$  are from Greve *et al.* <sup>19</sup> and the experimental results for  $ScF_3$  are taken from Oba *et al.* <sup>49</sup>. The statistical uncertainty in our predictions is on par with the size of the symbols themselves, and thus error bars not shown.

show that CTE predictions for ScF<sub>3</sub> and CaZrF<sub>6</sub> with our simulation systems are converged with respect to supercell size. The remaining consideration is the accuracy of the underlying density functional, which is PBE in this study. In this regard, our predictions for ScF<sub>3</sub> thermal expansion are similar to the AIMD results from Bocharov *et al.* <sup>58</sup> that utilize the PBEsol functional (Figure S10), although predictions with PBEsol show a higher temperature for transition from negative to positive thermal expansion, in better agreement with experiment. Dispersion corrected functionals would potentially be expected to yield better physical predictions. In fact, these were the initial functionals chosen for this study, but our initial NN models trained to dispersion corrected functionals all proved to exhibit dramatic instabilities when utilized in MD simulations (see Supplementary Material); similar issues have

been noted before.<sup>94</sup> An interesting direction for future work would be to examine an improved treatment of electron correlation through methods such as the random-phase approximation (RPA),<sup>94–96</sup> which may be achieved by either completely rebuilding the neural network/training set or possibly through a transfer learning procedure.<sup>97</sup>

Despite the quantitative errors, our NN-driven MD simulations represent the "state-of-the-art" in *ab initio*, equation of state predictions for ScF<sub>3</sub> and CaZrF<sub>6</sub>. Figure 1b compares alternative theoretical predictions for the CTE of ScF<sub>3</sub>. Specifically, we compare to predictions from the SCP and ISC phonon theories from Oba *et al.* <sup>49</sup>. The SCP theory goes beyond the quasiharmonic approximation (QHA) by incorporating quartic anharmonicity, and the ISC incorporates cubic anharmonicity. The predictions of SCP and ISC theories are

based on quantum mechanical free energy functions, and thus explicitly take into account NQEs. 49 Furthermore classical limits can be derived within the SCP framework, and we label such results from Oba et al. 49 as "Classical SCP" in Figure 1b. As indicated in Figure 1b, the shape of the classical SCP CTE curve looks similar to our classical MD and PIMD results; however the predictions exhibit significant quantitative deviation from experiment as they display essentially no NTE over the reported temperature range. Comparing the classical and quantum SCP results indicates a very similar contribution of NQEs as predicted by our classical MD/PIMD simulations. Of the theoretical models, the ISC predictions exhibit the best quantitative agreement with experiment, and show a similar temperature-dependent trend for CTE as compared to experiment. Overall, the ISC predictions and our "PI NN" predictions for CTE exhibit similar quantitative accuracy as compared to experiment. This indicates that including cubic and quartic anharmonicity within the ISC theory provides similar predictive accuracy as PIMD simulations for ScF<sub>3</sub> and similar materials. The methods should be viewed as complementary; PIMD provides a straightforward approach for property predictions utilizing standard DFT machinery (energy, forces and stress tensor), while the ISC phonon theory provides enhanced physical understanding of anharmonicity contributions to the equation of state behavior.<sup>49</sup>

We next compare atomic displacement parameters (ADPs), which measure the mean-square displacement of an atom from its crystal lattice position. 98 There are six unique components to the anisotropic atomic displacement tensor (three diagonal and three off-diagonal). 98 The mean-square displacement of each atom is straightforward to compute from simulations, e.g.  $U_{xx} = \langle u_x^2 \rangle$ , where u is an instantaneous atomic displacement from its mean position and x is a Cartesian coordinate. These can be compared to corresponding experimental values as measured by neutron or X-ray diffraction.<sup>98</sup> Within the ScF<sub>3</sub> crystal lattice, the Sc atoms undergo isotropic displacement,  $U_{iso} = U_{11} = U_{22} = U_{33}$ ; for F atoms, the displacement parameters corresponding to transverse motion  $(U_{11} = U_{22})$  are different from the displacement parameter corresponding to longitudinal motion  $(U_{33})$ . In Figure 2, we compare the atomic displacement parameters for ScF3 as predicted by our simulations to experimental values. 19 We first focus on the scandium atoms (Figure 2a). At low temperatures, the agreement between simulation and experiment is quite good. At higher temperatures, the simulations predict somewhat larger atomic displacement parameters for Sc than what is observed in experiment. For the fluorine atoms (Figure 2b) there is very good agreement between the predicted and experimental ADPs over the full temperature range. The transverse  $U_{11}$  parameter for fluorine is much larger, with a stronger temperature dependence compared to the longitudal  $U_{33}$  parameter. As discussed previously, <sup>22</sup> this is the expected behavior for the cubic crystal structure. We note that there is no significant difference between the "NN" and "PI NN" results for all predicted ADP values, indicating a negligible influence of NQE.

The ADPs for CaZrF<sub>6</sub>, shown in Figure 3, display similarly good agreement with experiment.<sup>33</sup> In this case,  $U_{iso} = U_{11} =$ 

 $U_{22} = U_{33}$  for both Ca and Zr. The fluorine ADPs are similar to those in ScF<sub>3</sub>, with two ADPs corresponding to transverse motion and one ADP corresponding to longitudinal motion. The fluorine ADPs within CaZrF<sub>6</sub> (Figure 3c) are somewhat larger than the corresponding ADPs in ScF<sub>3</sub>(note the different temperature scales of Figure 2 and Figure 3); this correlates with the more substantial NTE in CaZrF<sub>6</sub> as compared to ScF<sub>3</sub>. The agreement between the Ca and Zr ADPs in Figure 3a and b between simulation and experiment is good, although there is some slight disagreement at 100 K for Ca (Figure 3a). Analagous to ScF<sub>3</sub> there is no significant difference between the classical and path integral ADP predictions for CaZrF<sub>6</sub>, indicating negligible influence of NQE.

We next discuss pressure-volume equation of state predictions, as compared with experiment. ScF<sub>3</sub> is reported to undergo pressure-induced softening, which is an anomalous phenomenon that has been hypothesized to be driven by similar phonon mechanisms as NTE.<sup>22</sup> The Birch-Murnaghan equation of state provides information about the extent of pressure-induced softening observed over a given region of the phase diagram. The third-order Birch-Murnagahn equation of state is given by:

$$P(V) = \frac{3B_0}{2} \left[ \left( \frac{V_0}{V} \right)^{7/3} - \left( \frac{V_0}{V} \right)^{5/3} \right] \times \left\{ 1 + \frac{3}{4} (B' - 4) \left[ \left( \frac{V_0}{V} \right)^{2/3} - 1 \right] \right\}$$
(1)

There are three fitted quantities in Equation 1:  $B_0$  is the value of the bulk modulus at zero pressure,  $V_0$  is the value of the volume at zero pressure and B' is the first derivative of the bulk modulus with respect to pressure. A negative value of B' indicates pressure-induced softening. Figure 4a shows the pressure-volume curves from experiment,  $^{22}$  and Figure 4b shows our simulation predictions for the cubic phase of ScF<sub>3</sub>. Each data set was subsequently fit to Equation 1, with the fits corresponding to solid lines in Figure 4 and the fitted parameters  $B_0$  and B' plotted in Figure 5. Note that here we only show predictions from classical MD, as we observed little change in the results with PIMD.

We first discuss the predictions from our simulations of the ScF<sub>3</sub> cubic phase. As seen in Figure 4b, the Birch-Murnaghan equation of state fits our simulation data well; we show the same results plotted with the 0 K DFT result in Figure S14. The fitted  $B_0$  values from the equation of state, shown in Figure 5, fall within the range of those fit to the experimental data. The simulation predicted volumes are approximately 3% smaller than the corresponding experimental volumes, which is largely due to errors in DFT predicted bond lengths. However, there are other non-trivial differences between our simulation curves and the experimental curves. The experimental P-V curves (Figure 4a) display a significant curvature at higher pressure, corresponding to the reported pressure-induced softening effect.<sup>22</sup> The pressureinduced softening observed experimentally is most apparent for the low temperature data. In contrast, there are no signatures of pressure-induced softening in our simulations of cubic phase ScF<sub>3</sub>. As shown in Figure 4b, the simulated P-V curves all exhibit a close to linear relationship between pressure and volume, even at lower temperatures. This is reflected in the value of B' plotted in Figure 5b, in which simulation

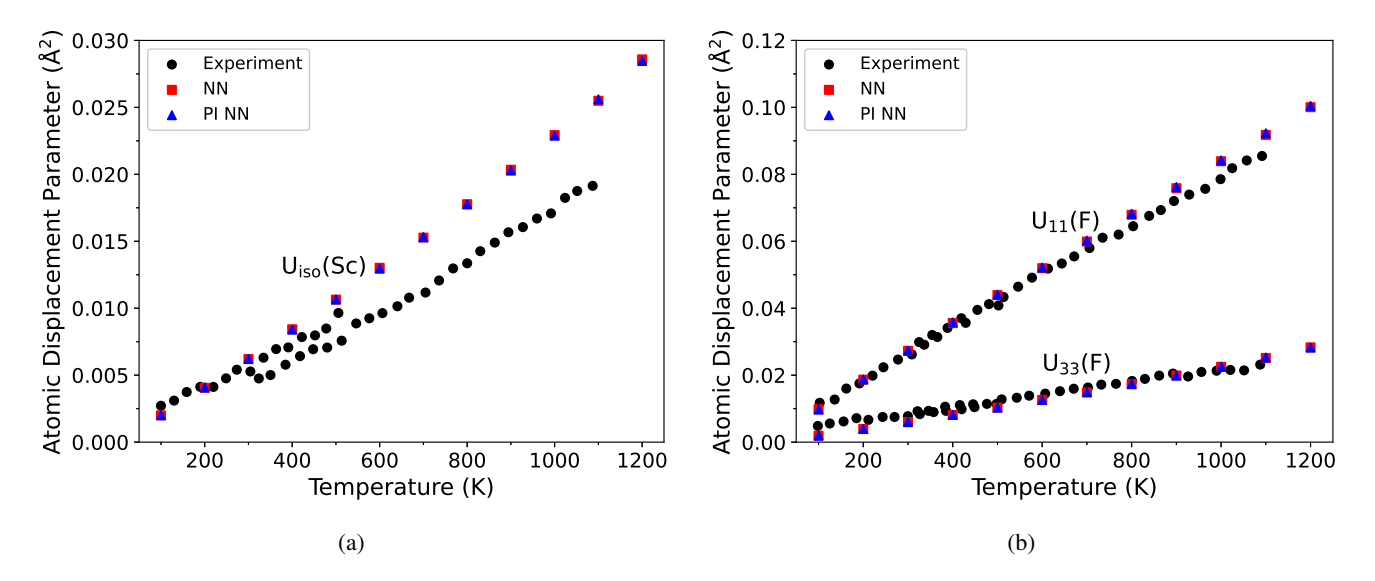


FIG. 2: ScF<sub>3</sub> atomic displacement parameters for a) Sc atoms ( $U_{iso}$ ) and b) F atoms ( $U_{11}$  and  $U_{33}$ ) The experimental data is from Greve *et al.* <sup>19</sup>. The statistical uncertainty in our predictions is on par with the size of the symbols themselves, and thus error bars not shown.

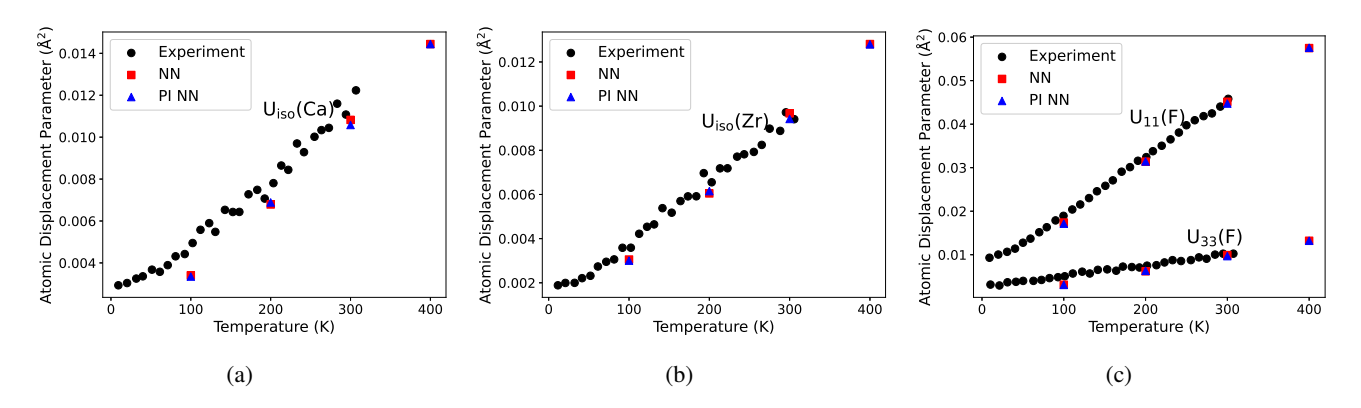


FIG. 3: CaZrF<sub>6</sub> atomic displacement parameter for a) Ca, b) Zr and c) F. The experimental data is from Hancock *et al.* <sup>33</sup>. The statistical uncertainty in our predictions is on par with the size of the symbols themselves, and thus error bars not shown.

values are all close to 0, reflecting no pressure-induced softening; in contrast, the experimental values are all significantly negative. The high pressure bound of the experimental P-V data in Figure 4a corresponds to a phase transition of ScF<sub>3</sub> from the cubic to rhombohedral phase. 19. It has thus been hypothesized that the pressure-induced softening effect is related to the proximity to this phase transition, and/or local fluctuations involving ScF<sub>6</sub> octahedral rotations that resemble motifs of the rhombohedral phase.<sup>22</sup> We thus speculated that the reason simulated P-V curves do not display pressure-induced softening was because the NN was trained solely to ScF3 cubic phase data, and does not "extrapolate" to such structural motifs. We hypothesized that by adding rhombohedral phase structures to the NN training set, the NN would "learn" about such rhombohedral-like, local ScF<sub>6</sub> octahedral rotations, possibly improving agreement with experiment. However, this hypothesis turned out to be false (at least in terms of improving agreement with experiment). Upon adding significant training data encompassing rhombohedral structures, and retraining the neural network, the simulation predictions were essentially unchanged (Figure S12 and S13).

At this point, we can only speculate on the discrepancy with experiment. The simulations of the ScF<sub>3</sub> cubic phase may not be capturing local fluctuations involving ScF<sub>6</sub> octahedral rotations that resemble motifs of the rhombohedral phase, and are an important mechanism for pressure induced softening. Of course, the (unknown) phase diagram of the DFT Hamiltonian is likely quantitatively different than the physical/experimental phase diagram of ScF<sub>3</sub>. If indeed the pressure-induced softening is related to close proximity to the phase-transition, then any discrepancy between DFT and experimental phase behavior would affect predictions of this phenomena. For example, if the cubic to rhombohedral transition occurred at much higher pressures on the DFT phase diagram, then the simulated pressures in Figure 4b may be relatively far from the phase-transition, possibly explaining the

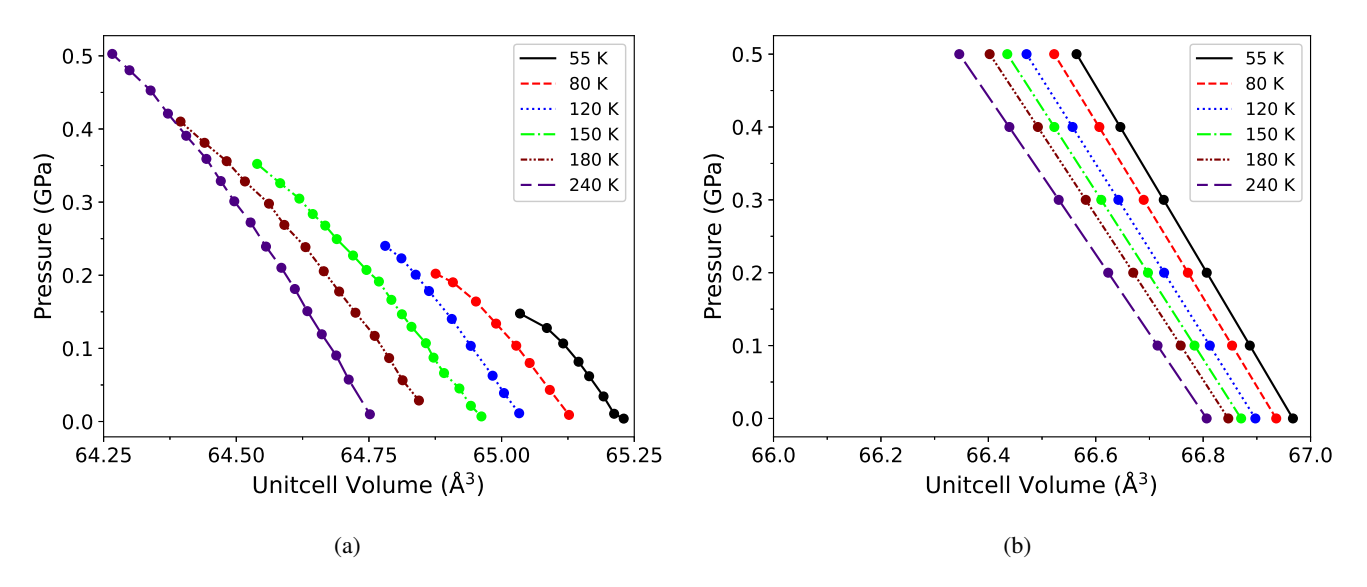


FIG. 4: a) Experimental pressure vs. volume data of ScF<sub>3</sub> from Wei *et al.* <sup>22</sup> b) Pressure vs. volume from the cubic ScF<sub>3</sub> simulations.

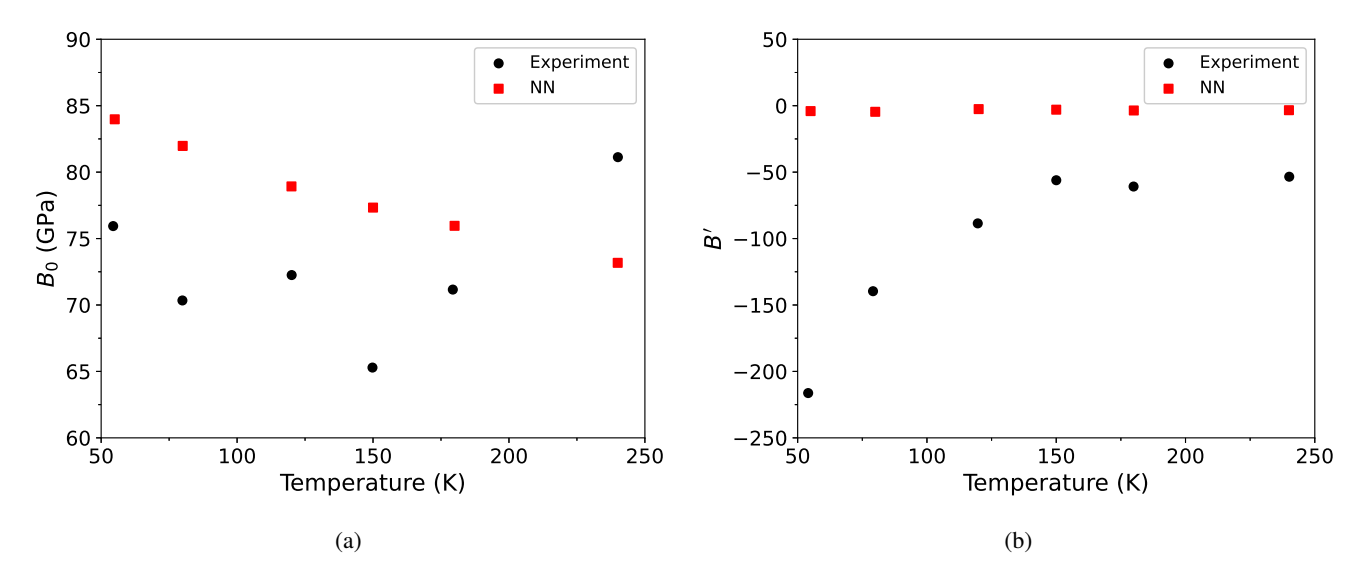


FIG. 5: a)  $B_0$  parameter and b) B' parameter from the Birch-Murnaghan equation of state from both simulation and experiment for ScF<sub>3</sub>. The experimental data is from Wei *et al.* <sup>22</sup>

lack of pressure-induced softening. This is entirely speculative, and would require characterization of the DFT-predicted phase behavior; however, such free energy calculations are beyond the scope of the present work. We note that previous MD simulations utilizing simple bond/angle potentials have predicted pressure-induced softening, in good qualitative agreement with experiment. However, the CTE predicted by these simulations were in large quantitative error, in contrast to our present *ab initio* predictions.

We next discuss equation of state and bulk modulus predictions for  $CaZrF_6$ . In Figure 6, we show experimental volume vs. pressure data for  $CaZrF_6$  at 290 K from Hester *et al.* <sup>34</sup>, as well as our corresponding predictions from the NN-driven

MD simulations (only classical MD results are shown, as NQE are minor here). There is very good agreement in the P-V trend as predicted by simulation compared to experiment. The absolute unitcell volumes from the NN simulations differ from the experimental values by about 3%, again due to corresponding error in DFT predicted bond lengths. Additionally, it is seen that there is essentially no pressure-induced softening for CaZrF<sub>6</sub> over this temperature/pressure range. In Figure 7, we compare simulation predictions of CaZrF<sub>6</sub> bulk modulus to experimental data over a wide temperature range.  $^{33}$  At STP, the predicted bulk modulus is 39 GPa, which is in excellent agreement with the experimental value of  $\sim$  37 GPa. The experimental bulk modulus indicates some thermal soft-

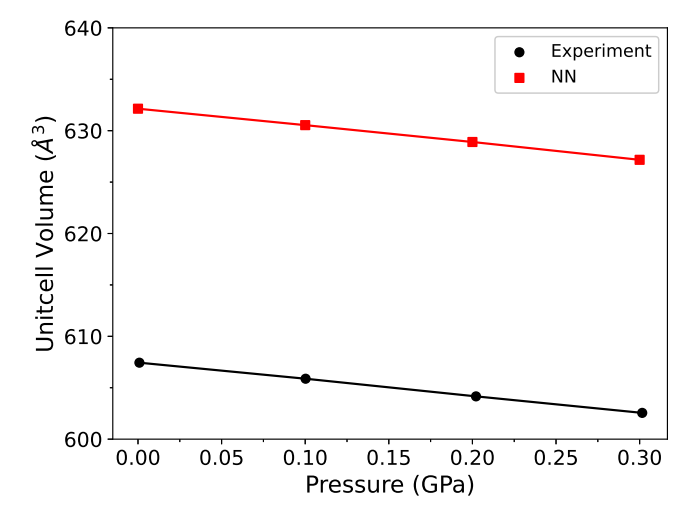


FIG. 6: CaZrF<sub>6</sub> Volume vs. Pressure data at 290K. The experimental data is from Hester *et al.* <sup>34</sup>

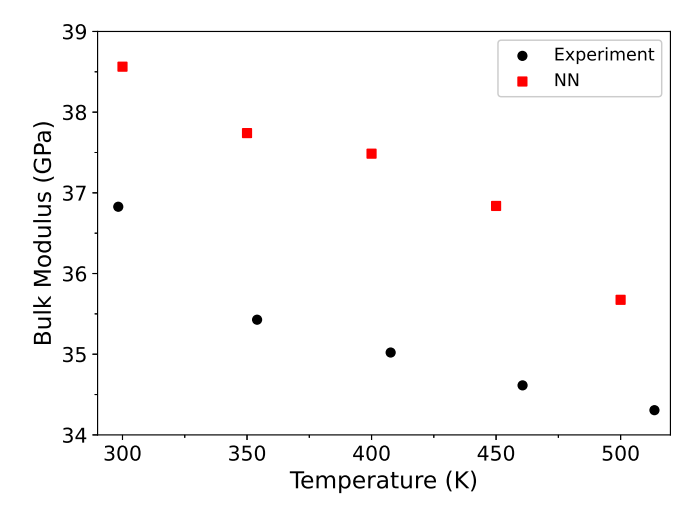


FIG. 7: CaZrF<sub>6</sub> Bulk modulus at various temperatures from both simulation and experiment. The experimental data is from Hancock *et al.* <sup>33</sup>

ening at higher temperatures, and our NN predictions follow a similar trend. Overall, the simulation predictions are in good agreement with experiment over the full temperature range.

## IV. CONCLUSION

We have demonstrated the accuracy attainable with DFT-trained NNs for predicting equation of state properties of the materials ScF<sub>3</sub> and CaZrF<sub>6</sub>. Our benchmarks have covered a representative set of properties for these systems, including the coefficient of thermal expansion, atomic displacement parameters, equations of state and the bulk modulus. Our NN-driven, MD simulation predictions largely follow the experimentally-observed trends. The advantage of the NN po-

tentials is that their development/parameterization is straight-forward utilizing modern software libraries, <sup>84,85</sup> and sufficient training data is generated from relatively short AIMD simulations. The enhanced computational efficiency of the NNs enable longer simulations of larger supercells compared to AIMD, and additionally allow application of path integral approaches for incorporating NQE.

Despite the state-of-the-art computational approach, we do not achieve the goal of quantitative accuracy in the equation of state predictions across the full temperature/pressure regime. In general, the NN-driven MD predictions agree better with experiment for pressure-volume properties such as the bulk modulus in comparison to CTE, although we are unable to reproduce the pressure-induced softening effect in ScF<sub>3</sub>. We have quantified the significant contribution of NOE to NTE at low temperatures; in general, classical simulations underpredict NQE in ScF3 and CaZrF6 at low temperature due to unphysical equipartition in high-frequency phonon modes with positive Grüneisen parameters. The NN potentials correctly predict that CaZrF<sub>6</sub> undergoes NTE to a greater extent than ScF<sub>3</sub>, and overall the predictions exhibit semiquantitative to qualitative agreement with experiment. However, even with PIMD, the CTE is underestimated in magnitude in comparison to the experimental values, showing that there is other missing physics. In addition, the predicted turnover from negative to positive thermal expansion occurs at too low a temperature for both materials. To improve the predictions, it is likely necessary to go beyond the GGA density functional description of electron correlation, e.g. utilizing more accurate RPA or many-body methods.<sup>99</sup> An interesting direction for future work would be to compare predictions from a NN potential trained to a database generated from a higher-level of ab initio theory, such as RPA, to investigate whether better agreement with experiment could be attained. This may be most easily achieved through "transfer learning" of the present NN potentials to higher accuracy training data.<sup>97</sup> A similar procedure has been shown to work well for material property prediction. 100,101

Our approach has utility for further study of NTE materials, despite the noted deficiencies in quantitative predictions. Concerning future outlook, our workflow based on NN potentials provides the opportunity to investigate new materials for pronounced NTE. The results here show that trends in NTE between different compounds are correctly predicted, although this will require further testing and validation. A database of the results and structures from these NN simulations would help identify and analyze the important features necessary for strong NTE, which could also guide experiment. Additionally, it is possible to extend our simulations in order to incorporate defects or impurities into the framework, which has been done experimentally in order to tune NTE behavior. 25–27,35,38 Through these efforts, we anticipate that NN-driven, MD simulations will continue to play an increasingly important role in "first-principles" materials property predictions.

#### V. SUPPLEMENTARY MATERIAL

See the Supplementary Material for benchmarks for the kinetic energy cutoff used in the DFT calculations vs. internal pressure, a description of the loss function used, benchmarks for the neural network predicted energies and forces vs. DFT, benchmarks for the barostat used in this paper vs. other barostats, the ScF<sub>3</sub> NTE curves calculated with different supercell sizes, a comparison of the ScF<sub>3</sub> NTE curve vs. AIMD results, ScF<sub>3</sub> lattice constant values for classical vs path integral MD, ScF<sub>3</sub> pressure-volume equations of state, CaZrF<sub>6</sub> NTE curves from simulations of different supercell sizes, CaZrF<sub>6</sub> lattice constant values for classical vs. path integral MD and ScF<sub>3</sub> NN results for various properties when trained with various dispersion corrections. The input files with all hyperparameters used to build the DeepMD models are included as download "deepmd train files.zip". Additionally, all numerical data for manuscript figures are included as download "figures\_data.zip".

#### **ACKNOWLEDGMENTS**

APW acknowledges financial support under NSF DMR-2002739. This work used the Hive cluster, which is supported by the National Science Foundation under grant number 1828187. This research was supported in part through research cyberinfrastructure resources and services provided by the Partnership for an Advanced Computing Environment (PACE) at the Georgia Institute of Technology, Atlanta, Georgia, USA. We wish to thank an anonymous reviewer for pointing out the fact that simulations with odd number of unit cells for ScF<sub>3</sub> may not entirely capture phonons associated with tilt modes along the *M-R* branch.

#### DATA AVAILABILITY STATEMENT

The data that support the findings of this study are available from the corresponding author upon reasonable request.

- <sup>1</sup>A. Jain, S. P. Ong, G. Hautier, W. Chen, W. D. Richards, S. Dacek, S. Cholia, D. Gunter, D. Skinner, G. Ceder, and K. A. Persson, "Commentary: The Materials Project: A materials genome approach to accelerating materials innovation," APL Mater. 1, 011002 (2013).
- <sup>2</sup>A. R. Oganov, C. J. Pickard, Q. Zhu, and R. J. Needs, "Structure prediction drives materials discovery," Nature Reviews Materials 4, 331–348 (2019).
- <sup>3</sup>E. Kiely, R. Zwane, R. Fox, A. M. Reilly, and S. Guerin, "Density functional theory predictions of the mechanical properties of crystalline materials," CrystEngComm **23**, 5697–5710 (2021).
- <sup>4</sup>A. Jain, Y. Shin, and K. A. Persson, "Computational predictions of energy materials using density functional theory," Nature Reviews Materials 1, 1–13 (2016).
- <sup>5</sup>C. J. Bartel, "Review of computational approaches to predict the thermodynamic stability of inorganic solids," Journal of Materials Science 57, 10475–10498 (2022).
- <sup>6</sup>W. Sun, C. J. Bartel, E. Arca, S. R. Bauers, B. Matthews, B. Orvañanos, B.-R. Chen, M. F. Toney, L. T. Schelhas, W. Tumas, J. Tate, A. Zakutayev, S. Lany, A. M. Holder, and G. Ceder, "A map of the inorganic ternary metal nitrides," Nature Materials 18, 732–739 (2019), number: 7 Publisher: Nature Publishing Group.

- <sup>7</sup>Q. Li, K. Lin, Z. Liu, L. Hu, Y. Cao, J. Chen, and X. Xing, "Chemical Diversity for Tailoring Negative Thermal Expansion," Chem. Rev. 122, 8438–8486 (2021).
- <sup>8</sup>G. Ventura and M. Perfetti, *Thermal Properties of Solids at Room and Cryogenic Temperatures*, International Cryogenics Monograph Series (Springer Netherlands, Dordrecht, 2014).
- <sup>9</sup>G. Hartwig, Polymer Properties at Room and Cryogenic Temperatures, International Cryogenics Monograph Series (Springer US, 1994).
- <sup>10</sup>Y. Rong, M. Li, J. Chen, M. Zhou, K. Lin, L. Hu, W. Yuan, W. Duan, J. Deng, and X. Xing, "Large negative thermal expansion in non-perovskite lead-free ferroelectric Sn<sub>2</sub>P<sub>2</sub>S<sub>6</sub>," Phys. Chem. Chem. Phys. 18, 6247–6251 (2016).
- <sup>11</sup>D. Dubbeldam, K. S. Walton, D. E. Ellis, R. Q. Snurr, . D. Dubbeldam, R. Q. Snurr, K. S. Walton, and D. E. Ellis, "Exceptional Negative Thermal Expansion in Isoreticular Metal—Organic Frameworks," Angew. Chem. Int. Ed. 46, 4496–4499 (2007).
- <sup>12</sup>M. K. Gupta, B. Singh, R. Mittal, S. Rols, and S. L. Chaplot, "Lattice dynamics and thermal expansion behavior in the metal cyanides MCN (M=Cu, Ag, Au): Neutron inelastic scattering and first-principles calculations," Phys. Rev. B 93, 134307 (2016).
- <sup>13</sup>P. J. Attfield, "Mechanisms and materials for NTE," Front. Chem. 6, 371 (2018).
- <sup>14</sup>T. A. Mary, J. S. Evans, T. Vogt, and A. W. Sleight, "Negative Thermal Expansion from 0.3 to 1050 Kelvin in ZrW<sub>2</sub>O<sub>8</sub>," Science 272, 90–92 (1996).
- <sup>15</sup>J. S. Evans, T. A. Mary, and A. W. Sleight, "Negative thermal expansion materials," Physica B: Condens. Matter 241-243, 311–316 (1997).
- <sup>16</sup>T. Chatterji, T. C. Hansen, M. Brunelli, and P. F. Henry, "Negative thermal expansion of ReO<sub>3</sub> in the extended temperature range," Appl. Phys. Lett. **94**, 241902 (2009).
- <sup>17</sup>M. Dapiaggi and A. N. Fitch, "Negative (and very low) thermal expansion in ReO<sub>3</sub> from 5 to 300 K," J. Appl. Crystallogr. 42, 253–258 (2009).
- <sup>18</sup>J. Z. Tao and A. W. Sleight, "The role of rigid unit modes in negative thermal expansion," J. Solid State Chem. 173, 442–448 (2003).
- <sup>19</sup>B. K. Greve, K. L. Martin, P. L. Lee, P. J. Chupas, K. W. Chapman, and A. P. Wilkinson, "Pronounced Negative Thermal Expansion from a Simple Structure: Cubic ScF<sub>3</sub>," J. Am. Chem. Soc. **132**, 15496–15498 (2010).
- <sup>20</sup>B. J. Kennedy and T. Vogt, "Powder X-ray diffraction study of the rhombohedral to cubic phase transition in TiF<sub>3</sub>," Mater. Res. Bull. 37, 77–83 (2002).
- <sup>21</sup>S. Chaudhuri, P. J. Chupas, M. Wilson, P. Madden, and C. P. Grey, "Study of the nature and mechanism of the rhombohedral-to-cubic phase transition in  $\alpha$ -AlF<sub>3</sub> with molecular dynamics simulations," J. Phys. Chem. B **108**, 3437–3445 (2004).
- <sup>22</sup>Z. Wei, L. Tan, G. Cai, A. E. Phillips, I. Da Silva, M. G. Kibble, and M. T. Dove, "Colossal Pressure-Induced Softening in Scandium Fluoride," Phys. Rev. Lett. **124**, 255502 (2020).
- <sup>23</sup>C. Yang, P. Tong, J. C. Lin, X. G. Guo, K. Zhang, M. Wang, Y. Wu, S. Lin, P. C. Huang, W. Xu, W. H. Song, and Y. P. Sun, "Size effects on negative thermal expansion in cubic ScF<sub>3</sub>," Appl. Phys. Lett. **109**, 023110 (2016).
- <sup>24</sup>L. Hu, F. Qin, A. Sanson, L. F. Huang, Z. Pan, Q. Li, Q. Sun, L. Wang, F. Guo, U. Aydemir, Y. Ren, C. Sun, J. Deng, G. Aquilanti, J. M. Rondinelli, J. Chen, and X. Xing, "Localized Symmetry Breaking for Tuning Thermal Expansion in ScF<sub>3</sub> Nanoscale Frameworks," J. Am. Chem. Soc. **140**, 4477–4480 (2018).
- <sup>25</sup>C. R. Morelock, B. K. Greve, L. C. Gallington, K. W. Chapman, and A. P. Wilkinson, "Negative thermal expansion and compressibility of  $Sc_{1^{\circ}x}Y_xF_3$  ( $x \le 0.25$ )," J. Appl. Phys. **114**, 213501 (2013).
- <sup>26</sup>C. R. Morelock, L. C. Gallington, and A. P. Wilkinson, "Solid solubility, phase transitions, thermal expansion, and compressibility in Sc<sub>1-x</sub> Al<sub>x</sub> F<sub>3</sub>," J. Solid State Chem. **222**, 96–102 (2015).
- <sup>27</sup>C. R. Morelock, L. C. Gallington, and A. P. Wilkinson, "Evolution of negative thermal expansion and phase transitions in  $Sc_{1-x}Ti_xF_3$ ," Chem. Mater. **26**, 1936–1940 (2014).
- <sup>28</sup>F. Qin, J. Chen, U. Aydemir, A. Sanson, L. Wang, Z. Pan, J. Xu, C. Sun, Y. Ren, J. Deng, R. Yu, L. Hu, G. J. Snyder, and X. Xing, "Isotropic Zero Thermal Expansion and Local Vibrational Dynamics in (Sc,Fe)F<sub>3</sub>," Inorg. Chem. 56, 10840–10843 (2017).
- <sup>29</sup>L. Hu, J. Chen, L. Fan, Y. Ren, Y. Rong, Z. Pan, J. Deng, R. Yu, and X. Xing, "Zero thermal expansion and ferromagnetism in cubic

- $Sc_{1-x}M_xF_3$  (M = Ga, Fe) over a wide temperature range," J. Am. Chem. Soc. **136**. 13566–13569 (2014).
- <sup>30</sup>J. Chen, Q. Gao, A. Sanson, X. Jiang, Q. Huang, A. Carnera, C. G. Rodriguez, L. Olivi, L. Wang, L. Hu, K. Lin, Y. Ren, Z. Lin, C. Wang, L. Gu, J. Deng, J. P. Attfield, and X. Xing, "Tunable thermal expansion in framework materials through redox intercalation," Nat. Commun. 8, 1–7 (2017).
- <sup>31</sup>S. J. Baxter, K. V. Loske, A. J. Lloyd, and A. P. Wilkinson, "Controlling the Phase Behavior of Low and Negative Thermal Expansion ReO<sub>3</sub>-Type Fluorides using Interstitial Anions: Sc<sub>1-x</sub>Zr<sub>x</sub>F<sub>3+x</sub>," Inorg. Chem. **59**, 7188–7194 (2020).
- <sup>32</sup>T. Wang, J. Xu, L. Hu, W. Wang, R. Huang, F. Han, Z. Pan, J. Deng, Y. Ren, L. Li, J. Chen, and X. Xing, "Tunable thermal expansion and magnetism in Zr-doped ScF<sub>3</sub>," Appl. Phys. Lett. **109**, 181901 (2016).
- <sup>33</sup>J. C. Hancock, K. W. Chapman, G. J. Halder, C. R. Morelock, B. S. Kaplan, L. C. Gallington, A. Bongiorno, C. Han, S. Zhou, and A. P. Wilkinson, "Large Negative Thermal Expansion and Anomalous Behavior on Compression in Cubic ReO<sub>3</sub>-Type A<sup>I</sup>IB<sup>I</sup>VF<sub>6</sub>: CaZrF<sub>6</sub> and CaHfF<sub>6</sub>," Chem. Mater. 27, 3912–3918 (2015).
- <sup>34</sup>B. R. Hester, A. M. Dos Santos, J. J. Molaison, J. C. Hancock, and A. P. Wilkinson, "Synthesis of Defect Perovskites (He<sub>2−x</sub> □ <sub>x</sub>)(CaZr)F<sub>6</sub> by Inserting Helium into the Negative Thermal Expansion Material CaZrF<sub>6</sub>," J. Am. Chem. Soc. **139**, 13284–13287 (2017).
- <sup>35</sup>A. J. Lloyd, B. R. Hester, S. J. Baxter, S. Ma, V. B. Prakapenka, S. N. Tkachev, C. Park, and A. P. Wilkinson, "Hybrid Double Perovskite Containing Helium: [He<sub>2</sub>][CaZr]F<sub>6</sub>," Chem. Mater. 33, 3132–3138 (2021).
- <sup>36</sup>C. A. Occhialini, S. U. Handunkanda, E. B. Curry, and J. N. Hancock, "Classical, quantum, and thermodynamics of a lattice model exhibiting structural negative thermal expansion," Phys. Rev. B 95, 094106 (2017).
- <sup>37</sup>T. A. Bird, J. Woodland-Scott, L. Hu, M. T. Wharmby, J. Chen, A. L. Goodwin, and M. S. Senn, "Anharmonicity and scissoring modes in the negative thermal expansion materials ScF<sub>3</sub> and CaZrF<sub>6</sub>," Phys. Rev. B 101, 064306 (2020).
- <sup>38</sup>F. Han, L. Hu, Z. Liu, Q. Li, T. Wang, Y. Ren, J. Deng, J. Chen, and X. Xing, "Local structure and controllable thermal expansion in the solid solution (Mn<sub>1-x</sub>Ni<sub>x</sub>)ZrF<sub>6</sub>," Inorg. Chem. Front. 4, 343–347 (2017).
- <sup>39</sup>D. Wendt, E. Bozin, J. Neuefeind, K. Page, W. Ku, L. Wang, B. Fultz, A. V. Tkachenko, and I. A. Zaliznyak, "Entropic elasticity and negative thermal expansion in a simple cubic crystal," Sci. Adv. 5 (2019), 10.1126/SCI-ADV.AAY2748/SUPPL\_FILE/AAY2748\_SM.PDF.
- <sup>40</sup>L. Wang, C. Wang, Y. Sun, S. Deng, K. Shi, H. Lu, P. Hu, and X. Zhang, "First-Principles Study of  $Sc_{1-x}Ti_xF_3$  ( $x \le 0.375$ ): Negative Thermal Expansion, Phase Transition, and Compressibility," J. Am. Ceram. Soc. **98**, 2852–2857 (2015).
- <sup>41</sup> V. Heine, P. R. Welche, and M. T. Dove, "Geometrical Origin and Theory of Negative Thermal Expansion in Framework Structures," J. Am. Ceram. Soc. 82, 1793–1802 (1999).
- <sup>42</sup>A. P. Giddy, M. T. Dove, G. S. Pawley, and V. Heine, "The determination of rigid-unit modes as potential soft modes for displacive phase transitions in framework crystal structures," Acta Crystallographica Section A: Foundations of Crystallography 49, 697–703 (1993), number: 5 Publisher: International Union of Crystallography.
- <sup>43</sup>M. T. Dove and H. Fang, "Negative thermal expansion and associated anomalous physical properties: review of the lattice dynamics theoretical foundation," Reports on Progress in Physics 79, 066503 (2016), publisher: IOP Publishing.
- <sup>44</sup>K. D. Hammonds, M. T. Dove, A. P. Giddy, V. Heine, and B. Winkler, "Rigid-unit phonon modes and structural phase transitions in framework silicates," American Mineralogist 81, 1057–1079 (1996).
- <sup>45</sup>A. K. Pryde, K. D. Hammonds, M. T. Dove, V. Heine, J. D. Gale, and M. C. Warren, "Rigid unit modes and the negative thermal expansion in ZrW2O8," Phase Transitions 61, 141–153 (1997), publisher: Taylor & Francis \_eprint: https://doi.org/10.1080/01411599708223734.
- <sup>46</sup>M. T. Dove, Z. Wei, A. E. Phillips, D. A. Keen, and K. Refson, "Which phonons contribute most to negative thermal expansion in ScF3?" APL Materials 11, 041130 (2023).
- <sup>47</sup>M. T. Dove, J. Du, Z. Wei, D. A. Keen, M. G. Tucker, and A. E. Phillips, "Quantitative understanding of negative thermal expansion in scandium trifluoride from neutron total scattering measurements," Physical Review B 102, 094105 (2020), publisher: American Physical Society.

- <sup>48</sup> A. Sanson, M. Giarola, G. Mariotto, L. Hu, J. Chen, and X. Xing, "Lattice dynamics and anharmonicity of CaZrF6 from Raman spectroscopy and ab initio calculations," Materials Chemistry and Physics 180, 213–218 (2016), publisher: Elsevier Ltd.
- <sup>49</sup>Y. Oba, T. Tadano, R. Akashi, and S. Tsuneyuki, "First-principles study of phonon anharmonicity and negative thermal expansion in ScF<sub>3</sub>," Phys. Rev. Mater. 3, 033601 (2019).
- <sup>50</sup>S. Baroni, P. Giannozzi, and E. Isaev, "Density-Functional Perturbation Theory for Quasi-Harmonic Calculations," Rev. Mineral. Geochem. 71, 39–57 (2010).
- <sup>51</sup>C. W. Li, X. Tang, J. A. Muñoz, J. B. Keith, S. J. Tracy, D. L. Abernathy, and B. Fultz, "Structural relationship between negative thermal expansion and quartic anharmonicity of cubic ScF3," Phys. Rev. Lett. 107, 195504 (2011).
- <sup>52</sup>T. Tadano and S. Tsuneyuki, "Self-consistent phonon calculations of lattice dynamical properties in cubic SrTiO<sub>3</sub> with first-principles anharmonic force constants," Phys. Rev. B Condens. Matter Mater. Phys. **92**, 054301 (2015).
- <sup>53</sup>N. R. Werthamer, "Self-Consistent Phonon Formulation of Anharmonic Lattice Dynamics," Phys. Rev. B 1, 572 (1970).
- <sup>54</sup> V. V. Goldman, G. K. Horton, and M. L. Klein, "An Improved Self-Consistent Phonon Approximation," Phys. Rev. Lett. 21, 1527 (1968).
- <sup>55</sup>F. Zhou, W. Nielson, Y. Xia, and V. Ozolinš, "Compressive sensing lattice dynamics. I. General formalism," Phys. Rev. B 100, 184308 (2019).
- <sup>56</sup>F. Zhou, B. Sadigh, D. Åberg, Y. Xia, and V. Ozolinš, "Compressive sensing lattice dynamics. II. Efficient phonon calculations and long-range interactions," Phys. Rev. B **100**, 184309 (2019).
- <sup>57</sup>P. Lazar, T. Bučko, and J. Hafner, "Negative thermal expansion of ScF<sub>3</sub>: Insights from density-functional molecular dynamics in the isothermalisobaric ensemble," Phys. Rev. B Condens. Matter Mater. Phys. **92**, 224302 (2015).
- <sup>58</sup>D. Bocharov, M. Krack, Y. Rafalskij, A. Kuzmin, and J. Purans, "Ab initio molecular dynamics simulations of negative thermal expansion in ScF<sub>3</sub>: The effect of the supercell size," Comput. Mater. Sci. **171**, 109198 (2020).
- <sup>59</sup>C. Wang, Q. Gao, a., M. Zhang, A. Doi, S. Shimano, T. Matsunaga, D. Bocharov, Y. Rafalskij, M. Krack, M. Putnina, and A. Kuzmin, "Negative thermal expansion of ScF<sub>3</sub>: first principles vs empirical molecular dynamics," in *IOP Conference Series: Materials Science and Engineering*, Vol. 503 (IOP Publishing, 2019) p. 012001.
- <sup>60</sup>M. K. Gupta, B. Singh, R. Mittal, and S. L. Chaplot, "Negative thermal expansion behavior in MZrF<sub>6</sub> (M=Ca,Mg,Sr): Ab initio lattice dynamical studies," Phys. Rev. B **98**, 014301 (2018).
- <sup>61</sup>N. Wang, J. Deng, J. Chen, and X. Xing, "Phonon spectrum attributes for the negative thermal expansion of MZrF<sub>6</sub> (M = Ca, Mn-Ni, Zn)," Inorg. Chem. Front. 6, 1022–1028 (2019).
- <sup>62</sup>L. Fiedler, K. Shah, M. Bussmann, and A. Cangi, "Deep dive into machine learning density functional theory for materials science and chemistry," Phys. Rev. Mater. 6, 040301 (2022).
- <sup>63</sup> V. L. Deringer, M. A. Caro, and G. Csányi, "Machine learning interatomic potentials as emerging tools for materials science," Advanced Materials 31, 1902765 (2019), https://onlinelibrary.wiley.com/doi/pdf/10.1002/adma.201902765.
- <sup>64</sup>J. Schmidt, M. R. Marques, S. Botti, and M. A. Marques, "Recent advances and applications of machine learning in solid-state materials science," npj Comput. Mater. 5, 1–36 (2019).
- <sup>65</sup>F. Noé, A. Tkatchenko, K. R. Müller, and C. Clementi, "Machine Learning for Molecular Simulation," Annu. Rev. Phys. Chem. 71, 361–390 (2020).
- <sup>66</sup>J. Behler, "Perspective: Machine learning potentials for atomistic simulations," J. Chem. Phys. **145**, 170901 (2016).
- <sup>67</sup>P. O. Dral, "Quantum Chemistry in the Age of Machine Learning," J. Phys. Chem. Lett. 11, 2336–2347 (2020).
- <sup>68</sup>J. Behler, R. Marton+ák, D. Donadio, and M. Parrinello, "Pressure-induced phase transitions in silicon studied by neural network-based meta-dynamics simulations," Phys. Status Solidi B 245, 2618–2629 (2008).
- <sup>69</sup>J. Behler and M. Parrinello, "Generalized Neural-Network Representation of High-Dimensional Potential-Energy Surfaces," Phys. Rev. Lett. 98, 146401 (2007).
- <sup>70</sup>H. Eshet, R. Z. Khaliullin, T. D. Kühne, J. Behler, and M. Parrinello, "Ab initio quality neural-network potential for sodium," Phys. Rev. B Condens.

- Matter Mater. Phys. 81, 184107 (2010).
- <sup>71</sup>C. Chen, Z. Deng, R. Tran, H. Tang, I. H. Chu, and S. P. Ong, "Accurate force field for molybdenum by machine learning large materials data," Phys. Rev. Matter. 1, 043603 (2017).
- <sup>72</sup>X. Chen, L. F. Wang, X. Y. Gao, Y. F. Zhao, D. Y. Lin, W. D. Chu, and H. F. Song, "Machine learning enhanced empirical potentials for metals and alloys," Comput. Phys. Commun. 269, 108132 (2021).
- <sup>73</sup>S. Ma and Z. P. Liu, "Machine learning potential era of zeolite simulation," Chem. Sci. 13, 5055–5068 (2022).
- <sup>74</sup>O. Tayfuroglu, A. Kocak, and Y. Zorlu, "A neural network potential for the IRMOF series and its application for thermal and mechanical behaviors," Phys. Chem. Chem. Phys. 24, 11882–11897 (2022).
- <sup>75</sup>P. Friederich, F. Häse, J. Proppe, and A. Aspuru-Guzik, "Machine-learned potentials for next-generation matter simulations," Nat. Mater. 20, 750–761 (2021).
- <sup>76</sup>Y. Liu, T. Zhao, W. Ju, and S. Shi, "Materials discovery and design using machine learning," J. Materiomics 3, 159–177 (2017).
- <sup>77</sup>S. Lin, Y. Wang, Y. Zhao, L. R. Pericchi, A. J. Hernández-Maldonado, and Z. Chen, "Machine-learning-assisted screening of pure-silica zeolites for effective removal of linear siloxanes and derivatives," J. Mater. Chem. A 8, 3228–3237 (2020).
- <sup>78</sup>C. Altintas, O. F. Altundal, S. Keskin, and R. Yildirim, "Machine Learning Meets with Metal Organic Frameworks for Gas Storage and Separation," J. Chem. Inf. Model. 61, 2131–2146 (2021).
- <sup>79</sup>P. Giannozzi, O. Baseggio, P. Bonfà, D. Brunato, R. Car, I. Carnimeo, C. Cavazzoni, S. De Gironcoli, P. Delugas, F. Ferrari Ruffino, A. Ferretti, N. Marzari, I. Timrov, A. Urru, and S. Baroni, "Quantum ESPRESSO toward the exascale," J. Chem. Phys. 152, 154105 (2020).
- <sup>80</sup> A. Hjorth Larsen, J. Jørgen Mortensen, J. Blomqvist, I. E. Castelli, R. Christensen, M. Dułak, J. Friis, M. N. Groves, B. Hammer, C. Hargus, E. D. Hermes, P. C. Jennings, P. Bjerre Jensen, J. Kermode, J. R. Kitchin, E. Leonhard Kolsbjerg, J. Kubal, K. Kaasbjerg, S. Lysgaard, J. Bergmann Maronsson, T. Maxson, T. Olsen, L. Pastewka, A. Peterson, C. Rostgaard, J. SchiØtz, O. Schütt, M. Strange, K. S. Thygesen, T. Vegge, L. Vilhelmsen, M. Walter, Z. Zeng, and K. W. Jacobsen, "The atomic simulation environment A Python library for working with atoms," J. Phys. Condens. Matter 29, 30 (2017).
- <sup>81</sup>J. P. Perdew, K. Burke, and M. Ernzerhof, "Generalized gradient approximation made simple," Phys. Rev. Lett. 77, 3865–3868 (1996).
- <sup>82</sup>A. Dal Corso, "Pseudopotentials periodic table: From H to Pu," Comput. Mater. Sci. 95, 337–350 (2014).
- <sup>83</sup>M. Parrinello and A. Rahman, "Polymorphic transitions in single crystals: A new molecular dynamics method," J. Appl. Phys. **52**, 7182 (1998).
- <sup>84</sup>H. Wang, L. Zhang, J. Han, and W. E, "DeePMD-kit: A deep learning package for many-body potential energy representation and molecular dynamics," Comput. Phys. Commun. 228, 178–184 (2018).
- 85 L. Zhang, J. Han, H. Wang, R. Car, and E. Weinan, "Deep Potential Molecular Dynamics: A Scalable Model with the Accuracy of Quantum Mechanics," Phys. Rev. Lett. 120, 143001 (2018).
- <sup>86</sup>L. Zhang, J. Han, H. Wang, W. Saidi, R. Car, and W. E, "End-to-end Symmetry Preserving Inter-atomic Potential Energy Model for Finite and Extended Systems," in *Advances in Neural Information Processing Systems*, Vol. 31 (2018) pp. 8024–8035.
- <sup>87</sup>T. A. Young, T. Johnston-Wood, V. L. Deringer, and F. Duarte, "A transferable active-learning strategy for reactive molecular force fields," Chem.

- Sci. 12, 10944-10955 (2021).
- <sup>88</sup>H. J. Berendsen, J. P. Postma, W. F. Van Gunsteren, A. Dinola, and J. R. Haak, "Molecular dynamics with coupling to an external bath," J. Chem. Phys. 81, 3684 (1998).
- <sup>89</sup>G. Bussi, T. Zykova-Timan, and M. Parrinello, "Isothermal-isobaric molecular dynamics using stochastic velocity rescaling," J. Chem. Phys. 130, 074101 (2009).
- <sup>90</sup>G. J. Martyna, D. J. Tobias, and M. L. Klein, "Constant pressure molecular dynamics algorithms," J. Chem. Phys. **101**, 4177 (1998).
- <sup>91</sup>M. Ceriotti, J. More, and D. E. Manolopoulos, "i-PI: A Python interface for ab initio path integral molecular dynamics simulations," Comput. Phys. Commun. 185, 1019–1026 (2014).
- <sup>92</sup> V. Kapil, M. Rossi, O. Marsalek, R. Petraglia, Y. Litman, T. Spura, B. Cheng, A. Cuzzocrea, R. H. Meißner, D. M. Wilkins, B. A. Helfrecht, P. Juda, S. P. Bienvenue, W. Fang, J. Kessler, I. Poltavsky, S. Vandenbrande, J. Wieme, C. Corminboeuf, T. D. Kühne, D. E. Manolopoulos, T. E. Markland, J. O. Richardson, A. Tkatchenko, G. A. Tribello, V. Van Speybroeck, and M. Ceriotti, "i-PI 2.0: A universal force engine for advanced molecular simulations," Comput. Phys. Commun. 236, 214–223 (2019).
- <sup>93</sup>C. Wang, D. Chang, J. Wang, Q. Gao, Y. Zhang, C. Niu, C. Liu, and Y. Jia, "Size and crystal symmetry breaking effects on negative thermal expansion in ScF<sub>3</sub> nanostructures," Phys. Chem. Chem. Phys. 23, 24814–24822 (2021).
- <sup>94</sup>W. J. Kim, M. Kim, E. K. Lee, S. Lebègue, and H. Kim, "Failure of Density Functional Dispersion Correction in Metallic Systems and Its Possible Solution Using a Modified Many-Body Dispersion Correction," J. Phys. Chem. Lett. 7, 3278–3283 (2016).
- <sup>95</sup>A. Tkatchenko, R. A. Distasio, R. Car, and M. Scheffler, "Accurate and efficient method for many-body van der Waals interactions," Phys. Rev. Lett. 108, 236402 (2012).
- <sup>96</sup>G. P. Chen, V. K. Voora, M. M. Agee, S. G. Balasubramani, and F. Furche, "Random-Phase Approximation Methods," Annu. Rev. Phys. Chem. 68, 421–445 (2017).
- <sup>97</sup>C.-K. Lee, C. Lu, Y. Yu, Q. Sun, C.-Y. Hsieh, S. Zhang, Q. Liu, and L. Shi, "Transfer learning with graph neural networks for optoelectronic properties of conjugated oligomers," J. Chem. Phys. **154**, 024906 (2021).
- <sup>98</sup> K. N. Trueblood, H. B. Bürgi, H. Burzlaff, J. D. Dunitz, C. M. Gramaccioli, H. H. Schulz, U. Shmueli, and S. C. Abrahams, "Atomic Displacement Parameter Nomenclature. Report of a Subcommittee on Atomic Displacement Parameter Nomenclature," Acta. Cryst. **52**, 770–781 (1996).
- <sup>99</sup>N. Marzari, A. Ferretti, and C. Wolverton, en"Electronic-structure methods for materials design," Nature Materials 20, 736–749 (2021), number: 6 Publisher: Nature Publishing Group.
- <sup>100</sup>P. Liu, C. Verdi, F. Karsai, and G. Kresse, "Phase transitions of zirconia: Machine-learned force fields beyond density functional theory," Physical Review B 105, L060102 (2022), publisher: American Physical Society.
- <sup>101</sup>P. Liu, J. Wang, N. Avargues, C. Verdi, A. Singraber, F. Karsai, X.-Q. Chen, and G. Kresse, "Combining Machine Learning and Many-Body Calculations: Coverage-Dependent Adsorption of CO on Rh(111)," Physical Review Letters 130, 078001 (2023), publisher: American Physical Society.